Journal of the Earth and Space Physics, Vol. 46, No. 4, Winter 2021, P. 131-145 (Research)

DOI: 10.22059/jesphys.2020.298815.1007197

3D Gravity Cross-Correlation Imaging for Large Scale Data Analysis: Application to the Crustal Structure of Iran

Ahmadi, I.[1], Ghorbani, A.[2*] and Ansari, A. H.[2]

1. Ph.D. Student, Department of Mining and Metallurgical Engineering, Yazd University, Yazd, Iran
2. Associate Professor. Department of Mining and Metallurgical Engineering, Yazd University, Yazd, Iran

(Received: 9 March 2020, Accepted: 29 Sep 2020)

Abstract

We propose the 3D gravity cross-correlation method to large scale data analyses as a fast analysis method to image the underground mass distribution. This method presents the cross-correlation product of the observed gravity anomaly (or its vertical gradient) and the calculated field due to an elementary mass contrast source. The cross-correlation product of the domain is used to highlight the zones of the highest probability of mass concentrations. First, some synthetic examples demonstrate the reliability and resolution of the method. The synthetic models discover different parameters of investigation space as space dimensions and densities. Tests with synthetic bodies show that the resultant correlation coefficients of the approach can delineate causative bodies in the subsurface. Finally, terrestrial gravity anomaly data of Iran is used to study the crustal structure and the Moho depth of Iran. The result is in a good agreement compared with other research studies of the domain. This technique took about five minutes to calculate the 3D gravity cross-correlation of the whole terrestrial gravity data set of Iran (25,937 data) a computer. Hence, it can easily be used repeatedly to monitor changes of gravity field.

Keywords: Cross-Correlation, Gravity anomaly, Vertical gradient, Iran.

1. Introduction

Today, the gravity imaging method has an important and widespread role in many branches of earth science, such as tectonic studies, mineral exploration, gas and oil field exploration, environmental issues, and more. Airborne surveys can also be used when the topography is rough, or the study area is wide (Inácio and Gunter, 2010). Airborne vertical gravity gradient surveys have some advantages over the ground surveys. Gravitational gradients are less sensitive to aircraft altitude, they are also more accurate, and they require no correction, such as Bouguer correction (Alberts, 2009). The purpose of inverting the gravity data is to retrieve the geometrical and physical parameters of the buried mass depends on the purpose of the study.

There are two main approaches to 3D inversion of gravity data. In the first approach, the geometrical parameters of the model are kept constant by dividing the subsurface space into a grid of rectangular cells. In this case, the unknown density difference of each cell will be retrieved using some iterative optimization techniques (Bear et al., 1995; Braile et al., 1974; Li and Oldenburg, 1998). This method has an inherent problem called Non-uniqueness of solutions. In the second approach, the density difference is assumed to be stable, and unknown geometrical parameters of the model are estimated, such as in Talwani and Ewing (1960), Cordell and Henderson (1968), Oldenberg (1974), Gomez-Ortiz and Agarwal (2005), Chakravarthi and Sundararajan (2007). However, this approach also has the inherent non-uniqueness problem. In addition to the uniqueness of the solutions, all of the above-mentioned methods have another problem, they are very time-consuming and require a lot of computer memory.

The 3D gravity cross-correlation approach is an imaging method for estimating the equivalent physical property distribution of the subsurface in a probabilistic sense, without any external constraints and any linearization. This method was first introduced by Patella (1997) to analyze Spontaneous Potential (SP) data to locate subsurface anomalies. Mauriello and Patella (1999a, 1999b) tested this method in natural-source electromagnetic induction fields and resistivity data. Mauriello and Patella (2001) then applied this method to gravity data to

*Corresponding author: aghorbani@yazd.ac.ir

estimate the volume of buried masses. This method has also been used for multipole SP sources to determine possible locations of their centers and boundaries (Alaia et al., 2009). In a subsequent study by Guo et al. (2011), this method was used for vertical gravity gradient.

Previous studies have shown that using this approach is simple, easy to run, stable with low requirements of RAM of a computer, and less sensitive to noise. Also, this approach can be used for imaging large-scale observed dataset in a stable manner. The approach is suited to be used in the early phases of the interpretation process for an early evaluation of the subsurface source distribution, especially when no or little a priori information is available (Guo et al., 2010).

In this paper, we study the crustal structure and the Moho depth of Iran by applying the 3D gravity cross-correlation method on terrestrial gravity anomaly data of Iran. Thus, first we apply the 3D cross correlation method to Bouguer anomaly data, and Vertical Gravity Gradient (VGG). Some synthetic examples are also presented. Finally, the crustal structure and the Moho depth of Iran will be discussed by applying this method to the entire Bouguer anomaly data of Iran.

2. Methodology

In this section, we present the methodology. The survey is carried out on the (x, y) plane parallel to the sea level, and the z-axis is assumed positive downwards. For the prism element of our point mass, the Cartesian coordinate is Q=(x_q, y_q, z_q), its density difference $\Delta\sigma_q$, the volume of this element dv=dxdydz, and the survey is done at random station P=(x_i,y_i,z_i). The theoretical gravity anomaly value is calculated as follows (Pluff, 1976):

$$\Delta g_z(x_i, y_i, z_i) = \gamma \Delta\sigma_q \int_{a1}^{a2}\int_{b1}^{b2}\int_{z1}^{z2} \frac{zdzdydx}{r^3} \quad (1)$$

where a_i, b_i, z_i, and γ are the Cartesian coordinates of the vertices of the prism and the universal gravitation constant, respectively, and:

$$r = [(x-x')^2 + (y-y')^2 + (z-z')^2]^{\frac{1}{2}} \quad (2)$$

If the prism is considered as a cubic whose vertices are aligned with the coordinate system, Plouff (1976) has proposed the following formula for solving the above integral:

$$\Delta g_z = \gamma\Delta\sigma_q \sum_{i=1}^{2}\sum_{j=1}^{2}\sum_{k=1}^{2} s \begin{bmatrix} z_k \tan^{-1}\dfrac{a_i b_i}{z_k R_{ijk}} - \\ a_i \ln(R_{ijk} + b_i) - \\ b_i \ln(R_{ijk} + a_i) \end{bmatrix} \quad (3)$$

$$\Delta g_z = \gamma\Delta\sigma_q B_q(x_i, y_i, z_i)$$

where B_q (x_i, y_i, z_i) is called the geometrical function of mass Q for theoretical gravity anomaly at station P, and

$$R_{ijk} = [a_i^2 + b_j^2 + z_k^2]^{\frac{1}{2}} \quad (4)$$

And

$$s = s_i s_j s_k \text{ with } s_1 = -1, \text{ and } s_2 = +1 \quad (5)$$

Calculating the vertical derivative of Equation (1), the value of the theoretical vertical gravity gradient (VGG) at station P due to the cubic element Q is (Guo et al., 2010):

$$\Delta g_{z,q} = \gamma\Delta\sigma_q dv B_{z,q}(x_i, y_i, z_i) \quad (6)$$

where $B_{z,q}(x_i, y_i, z_i)$ is the geometrical function of the element Q for the gravity vertical gradient anomaly at station P, and its value after simplification is (Guo et al., 2010):

$$B_{z,q}(x_i, y_i, z_i) = \frac{2(z_q - z_i)^2 - (x_q - x_i)^2 - (y_q - y_i)^2}{[(x_q - x_i)^2 + (y_q - y_i)^2 + (z_q - z_i)^2]^{5/2}} \quad (7)$$

Now, to calculate the correlation between the observed gravity anomaly value and the theoretical gravity anomaly value due to the Q-cell, we have (Mauriello and Patella, 2001):

$$\eta_q = \frac{\sum_{i=1}^{N} \Delta g(x_i, y_i, z_i)\Delta g_z(x_i, y_i, z_i)}{\sqrt{\sum_{i=1}^{N} \Delta g^2(x_i, y_i, z_i) \sum_{i=1}^{N} \Delta g_z{}^2(x_i, y_i, z_i)}} \quad (8)$$

where N is the number of survey stations, and Δg is the observed gravity anomaly. By putting Equation (3) into Equation (8) we will have (Mauriello and Patella,2001):

$$\eta_q = \frac{\sum_{i=1}^{N} \Delta g(x_i, y_i, z_i) B_q(x_i, y_i, z_i)}{\sqrt{\sum_{i=1}^{N} \Delta g^2(x_i, y_i, z_i) \sum_{i=1}^{N} B_q{}^2(x_i, y_i, z_i)}} \quad (9)$$

η_q reflects the cross-correlation degree between the observed gravity anomaly and the theoretical gravity anomaly due to the element Q. By using the Cauchy-Schwarz inequality we have (Mauriello and Patella, 2001):

$$\left[\sum_{i=1}^{N} \Delta g(x_i, y_i, z_i) B_q(x_i, y_i, z_i)\right]^2 \leq \left[\sum_{i=1}^{N} \Delta g^2(x_i, y_i, z_i) \sum_{i=1}^{N} B_q{}^2(x_i, y_i, z_i)\right] \quad (10)$$

As a result, these values are always in the range of [-1, +1]. Similarly, for the VGG we have (Guo et al., 2010):

$$\eta_{z,q} = \frac{\sum_{i=1}^{N} \Delta g_z(x_i, y_i, z_i) B_{z,q}(x_i, y_i, z_i)}{\sqrt{\sum_{i=1}^{N} \Delta g_z{}^2(x_i, y_i, z_i) \sum_{i=1}^{N} B_{z,q}{}^2(x_i, y_i, z_i)}} \quad (11)$$

$\eta_{z,q}$ reflects the cross-correlation between the vertical gradient of observed gravity anomaly and the theoretical vertical gravity gradient due to the element Q. Similarly, by using the Cauchy-Schwarz inequality, values of $\eta_{z,q}$ are in the range of [-1, +1] too.

The values of $\eta_{z,q}$, and η_q (Equations (9) and (11)) indicate the probability that how much element Q is responsible for generating the observed data. Positive values of $\eta_{z,q}$, and η_q indicate the positive mass difference, and negative values of $\eta_{z,q}$ and η_q indicate the mass deficiency. The closer the absolute value of $\eta_{z,q}$ and η_q is to 1, the higher the probability of an excess or deficient mass (Patella, 1997; Mauriello and Patella, 1999a; Mauriello and Patella, 1999b; Mauriello and Patella, 2001; Alaia et al., 2009; Guo et al., 2010).

To perform the 3D cross-correlation process, the survey area must first be segmented into a 3D regular grid. Then, using the Equations (9) and (11), we can calculate the correlation coefficient between each node of this 3D network with the survey stations. In this article, after a few synthetic models, the gravity data of Iran will be studied.

3. Synthetic Examples

To analyze the ability of the 3D Cross-Correlation method, in this section, the method is tested on three different synthetic models, and its advantages and disadvantages are discussed.

3-1. 2 Cubes with Equal Density Difference

The first model consists of two cubes with a density difference of $\Delta\rho = 3 gr/cm^3$ relative to the field. The size of each cube is 200×100×50 m^3 along the x, y, and z axes, and the center of each cube is in the depth of 125 m underground. The distance between the stations and the profiles is 20m on a 1000×1000 m^2 area on the ground surface. Random Gaussian noise with a standard deviation of 5% was added to the data. Figure 1 shows the maps obtained from the observed gravity and the VGG. The black rectangles represent the location of the cubes on the (x, y) plane.

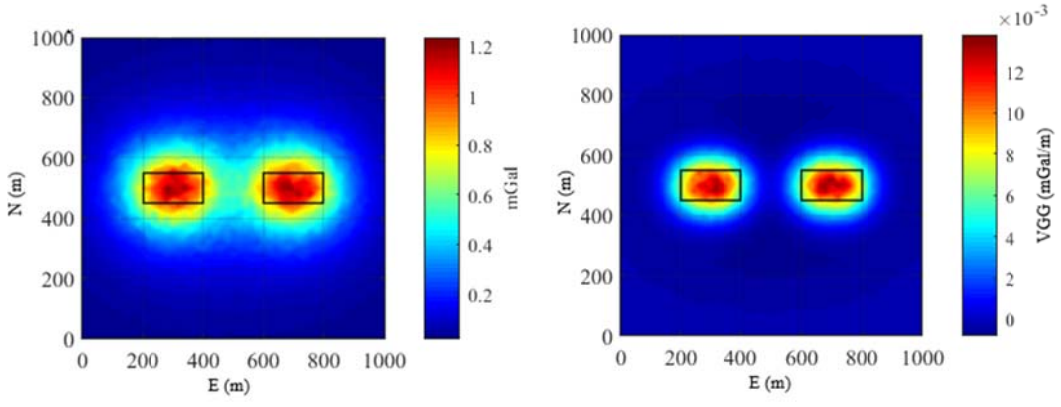

(a) (b)

Figure 1. a) Gravity anomaly map of masses with density difference 3 gr/cm^3. b) VGG map of masses with density difference of 3 gr/cm^3.

To perform the 3D Cross-Correlation process, the subsurface of the study area is segmented to a 3D grid network with dimensions of 1000×1000×300 m^3 in which the size of each cell is 20×20×10 m^3. Then the values of $\eta_{z,q}$, and η_q will be calculated for each cell of this network, and the results will be plotted. Figures 2 and 3 represent the results of applying this method on the gravity anomaly data and the vertical gravity gradient, respectively. As seen in the figures, the expansion and depth of the masses in both figures correspond well to the location with the highest values of $\eta_{z,q}$, and η_q.

3-2. 2 Cubes with Unequal Density Difference

To test the lateral resolution of cross-correlation method and to measure the sensitivity of this method to density changes, the second model consists of two cubes with density differences of $\Delta\rho = 3gr/cm^3$, and $\Delta\rho = 5gr/cm^3$ relative to the field. The size and location of both models are similar to the previous example. The survey was done similarly to the previous model, and Random Gaussian noise with a standard deviation of 5% was added to the data. Figure 4 shows the maps obtained from the gravity anomaly and VGG. The black cubes represent the location of the masses on the (x, y) plane.

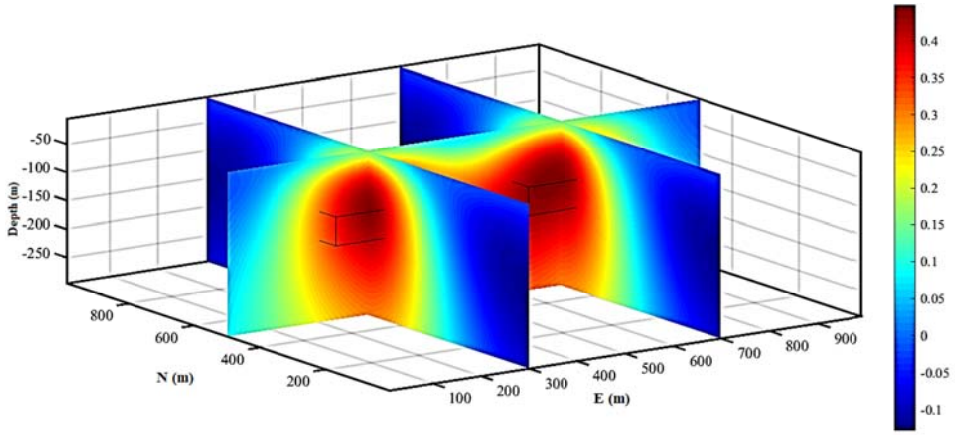

Figure 2. Map derived from the application of the 3D cross-correlation method on gravity data. Black lines show the outlines of the true prisms.

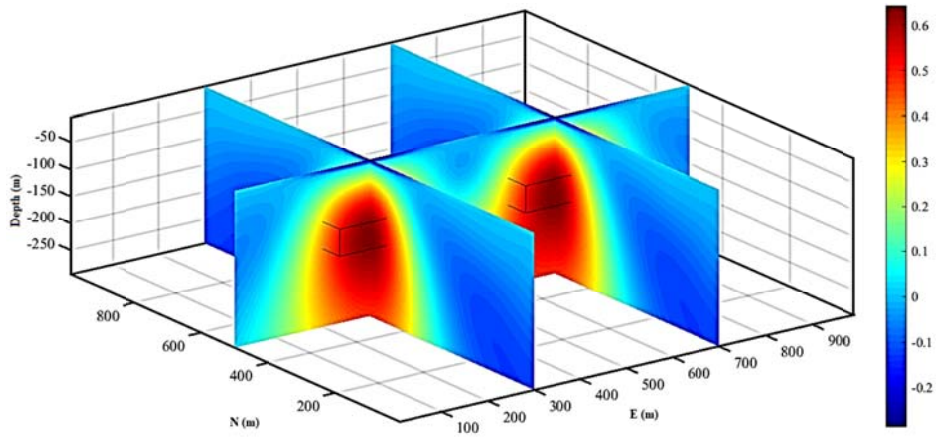

Figure 3. Map derived from applying the 3D cross-correlation method to VGG data. Black lines show the outlines of the true prisms.

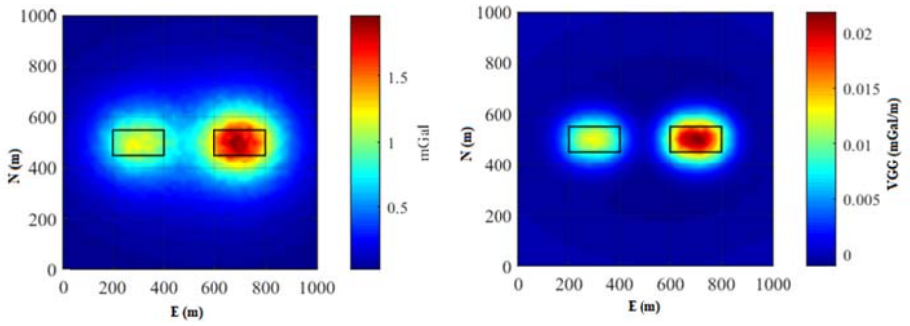

(a) (b)

Figure 4. a) Gravity anomaly map of two cubes with unequal density difference (left cube has the density difference of 3, and right has the density difference of 5 gr/m^3 relative to the field). b) VGG map of two cubes with the density difference of 3 and 5 gr/m^3.

In this case, like the previous model, to perform the 3D cross-correlation process, the subsurface of the study area is segmented to a 3D grid network with a dimension of 1000×1000×300 m^3 in which the size of each cell is 20×20×10 m^3. Then the values of $\eta_{z,q}$ and η_q were calculated for each cell of this network, and the results were plotted. Figure 5 (a), and Figure 6 (a) show the results of applying cross-correlation method on the observed gravity anomaly data, and VGG, respectively. To display the results of the tomography and resolution of this method better, the images of the x-z direction were also shown in Figure 5 (b) and Figure 6 (b). As seen, by applying the cross-correlation method on gravimetric data, only the buried mass and location with a density difference of 5 g/cm^3 can be recovered, and the lower density mass was seen as a part of mass with 5 g/cm^3. By applying this method on the data obtained from vertical gravity gradient, this problem has largely been resolved, and both buried masses are distinct and separable, but the center of the masses are not fully matched with the locations with the highest values. Considering the high speed of this method, the small cell size, and the low requirements of RAM of the computer on which the modelling operation is performed, results are remarkable.

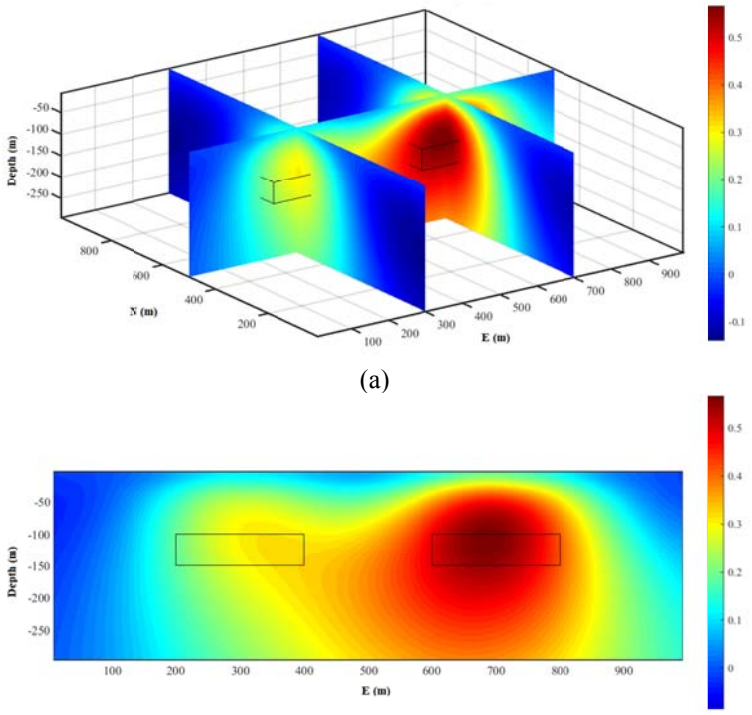

(a)

(b)

Figure 5. a) Map derived from the application of the 3D cross-correlation method to gravity data. Black lines show the outlines of the true prisms. b) The image in the x-z direction.

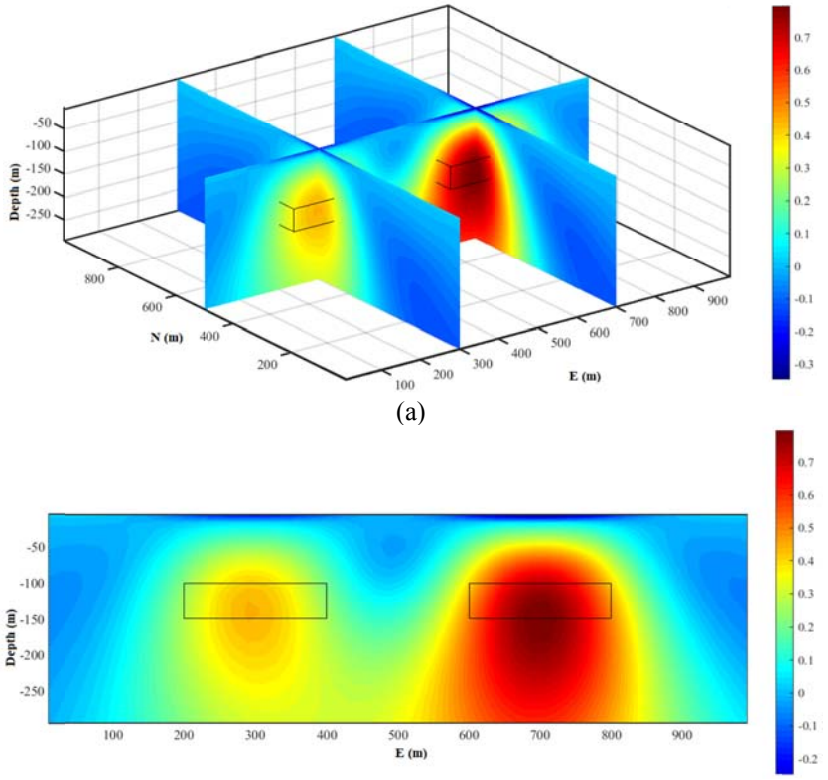

Figure 6. (a) Map derived from applying the 3D cross-correlation method to VGG data. Black lines show the outlines of the true prisms. (b) The image in the x-z direction.

3-3. 2 Cubes with Equal Density Difference and with Different Dimensions, and Depths

In this example, to test the lateral and in-depth resolution of the 3D cross-correlation, the model consists of two cubes with an equal density difference of $\Delta\rho = 3gr/cm^3$ relative to the field. Dimensions of the left cube is 100×100×50 m^3, and the center has a depth of 75 m, the right cube has dimensions of 250×150×50 m^3, and its center has a depth of 125 m. like the previous model, the distance between the stations, and profiles of the survey is 20 m on a 1000×1000 m^2 area on the ground surface. Random Gaussian noise with a standard deviation of 5% was added to the data. Figure 7 shows the maps obtained through the gravity and vertical gravity gradient survey. The black rectangles represent the location of the cubes on the (x, y) plane.

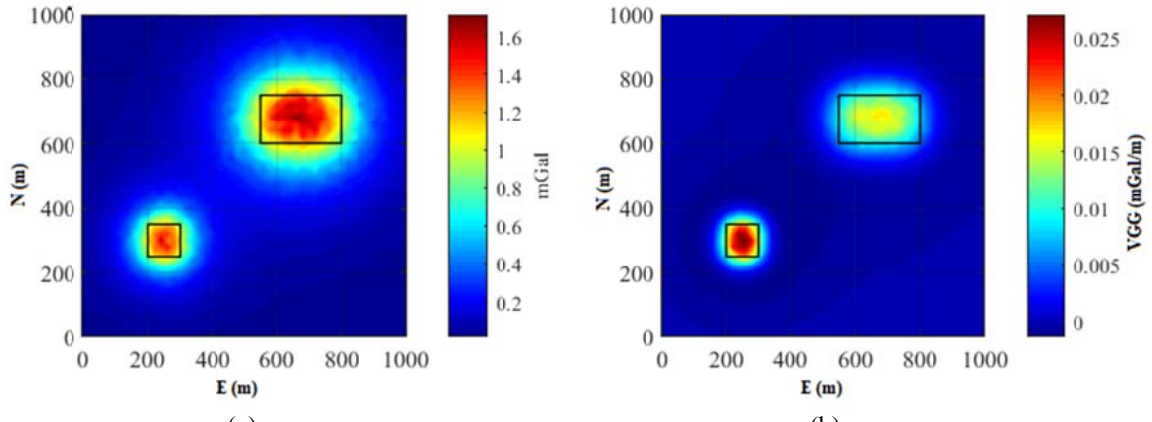

Figure 7. (a) Gravity anomaly map of two cubes with the density difference of 3 g/cm^3 at different depths. (b) VGG map.

To perform the cross-correlation process, the medium was divided to a 3D grid network with dimensions of 1000×1000×300 m^3 in which the size of each cell is 20×20×10 m^3. Then the values of $\eta_{z,q}$ and η_q were calculated for each cell of this network, and the results were plotted. Figures 8 and 9 show the results of cross-correlation on the gravity anomaly data and the VGG, respectively. As shown in Figures 8 and 9, the geometrical parameters of the masses in both images correspond well to the location with the highest probability, except that in Figure 8. The buried mass in Figure 8, near the surface, has less η_q values whereas it is quite distinct from the blue color field. In Figure 9, which is the result of applying the method to the VGG data, the geometrical parameters of these cubes are accordant with the areas with the highest $\eta_{z,q}$ values.

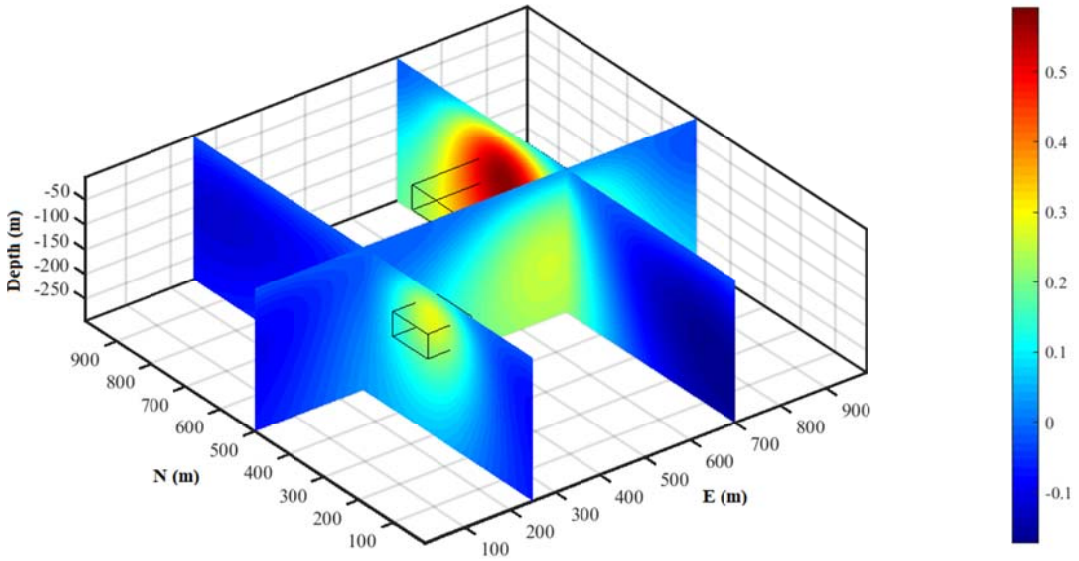

Figure 8. Map derived from the application of the 3D cross-correlation method to gravity data. Black lines show the outlines of the true prisms.

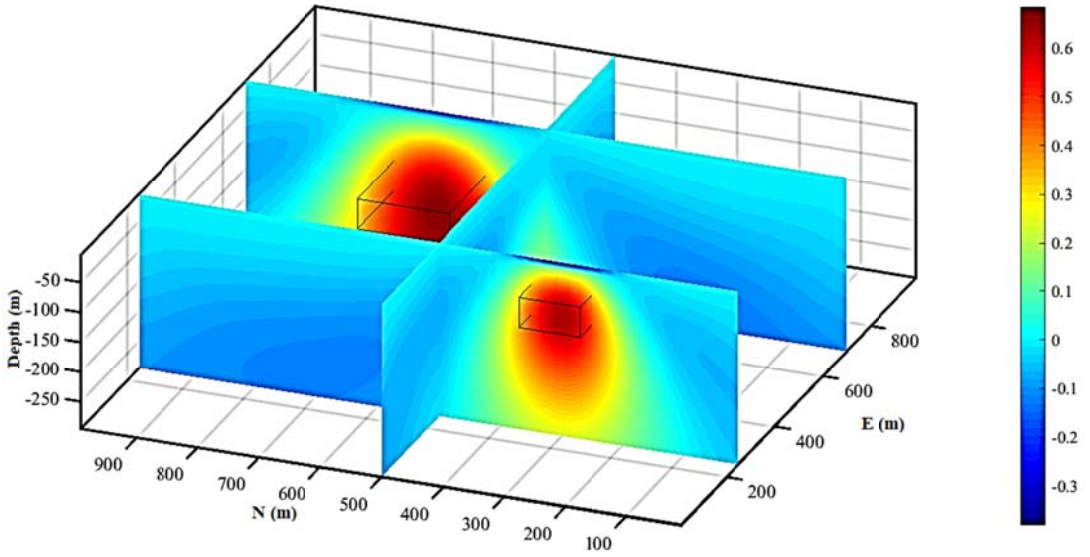

Figure 9. Map derived from applying the 3D cross-correlation method to VGG. Black lines show the outlines of the true prisms.

4. Field Data (Terrestrial Gravity Anomaly Data of Iran)

The terrestrial gravity anomaly data of Iran consists of 25937-observation point data. These data sets were collected from the National Oil Company of Iran, the Institute of Geophysics of the University of Tehran, and the Iran National Cartographic Center at different timescales (Figure 10). In this section, first, we discuss the tectonic, and orogeny of Iran's major geological zones briefly, and finally the results of applying the 3D cross-correlation method on terrestrial gravity anomaly data of Iran are presented.

The Iranian Plateau, part of the Alpine-Himalayan Tectonic Zone, is formed by the continental convergence between the Arabian, and Eurasian plates (Turan shield). Today, the Iranian plate is characterized by diverse tectonic domains including mountain belts (e.g., Zagros, Alborz and Kopeh-Dagh) and oceanic plate subduction (e.g., Makran) (Figure 11).

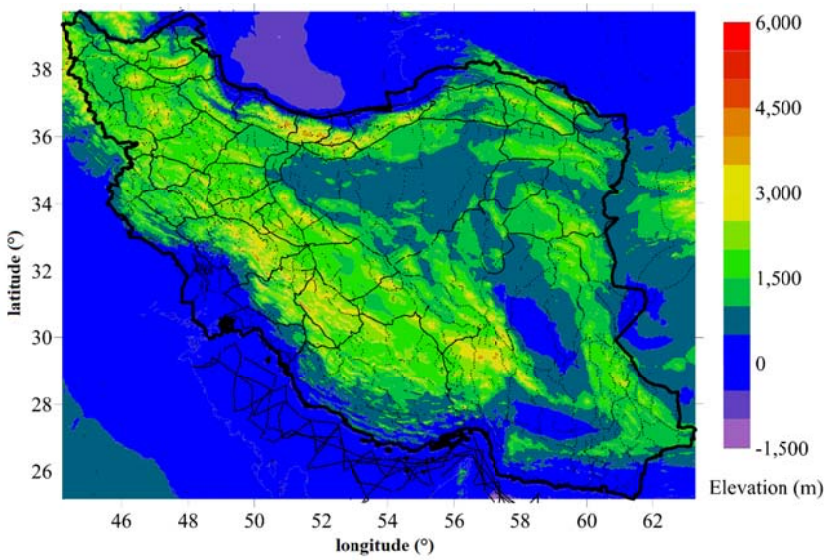

Figure 10. Location of terrestrial gravity anomaly data of Iran. Black dots represent the terrestrial gravity data observation points. The background map is SRTM 30 m of Iran.

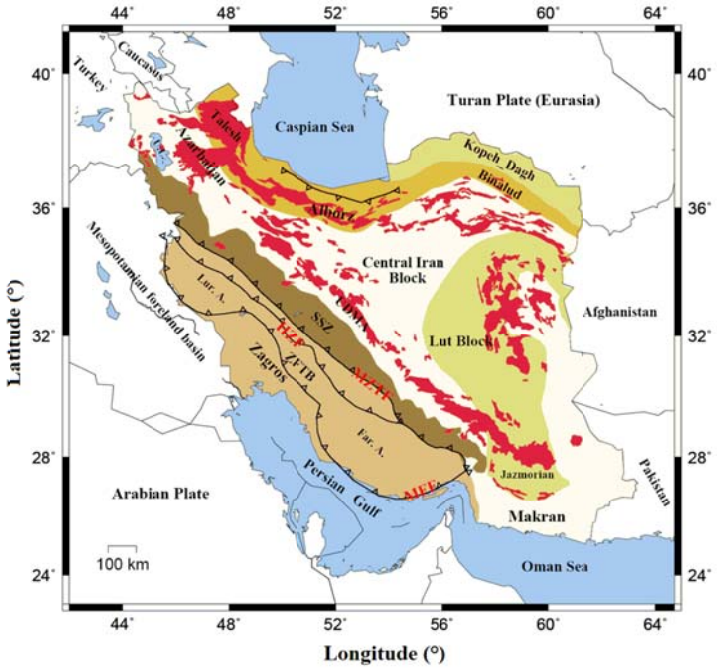

Figure 11. Simplified geological map of Iran showing the main tectonic subdivisions. UL: Urumieh Lake, SSZ: Sanandaj-Sirjan Zone, MZT: Main Zagros Thrust, ZFTB: Zagros Fold, and Thrust Belt, UDMA: Urumieh–Dokhtar Magmatic Arc (Taghizadeh-Farahmand et al., 2015).

The Zagros Folded Thrusting Belt (ZFTB) is the result of the convergence of the Arabian and Eurasian plates after the closure of the Young Tethys Ocean. After Zagros Zone, Sanandaj-Sirjan Zone (SSZ) can be mentioned, which forms the southwestern edge of Central Iran (CI), and is separated from the folded and thrust belt by the Main Zagros Thrust (MZT). SSZ is known by metamorphic formation. Many geologists consider the Urmia-Dokhtar Magmatic Arc (UDMA) as the NW boundary of the Sanandaj Sirjan Zone, which has the continuous volcanic activity (Berberian and King, 1981; Berberian, 1983).

The closure of the Neotethys Ocean resulted in the emplacement of ophiolites along the Zagros suture zone, and the onset of deformation in the Zagros fold, and thrust belt (Stoneley,1981; Richards et al., 2006). The collision process trapped the Central Iranian block between the Arabian plate in the south and the Turan shield (Kopeh Dagh) in the north, and led to intra-continental shortening, the formation of the Iranian plateau, widespread deformation, and mountain building (Bird, 1978). Alborz Zone is a region with high seismic activity, which is the result of the convergences of the Central Iran zone (to the north compared to Eurasia plate) and the southern basin of the Caspian Sea (to the west compared to Eurasia plate).

The Makran area in southeastern Iran and southern Pakistan is a section of the Eurasian-Arabian Plateau that extends from the Hormuz Strait in Iran to the Indus River mouth in Pakistan. In Makran, the oceanic part of the Arabian Plate is subducted beneath Eurasia along a subduction zone from the Early Cretaceous (Page et al., 1979).

Many studies have focused on bedrock characterization, the Moho discontinuity depth, the crustal structure, and tectonic status of different parts of Iran using airborne and terrestrial magnetic data, airborne and terrestrial gravity data, seismic, and teleseismic data. They have used various methods to model and process these data. In most of these studies, the goal was to determine the Moho depth and Upper Mantle Velocity Model in specific stations or several regions of Iran using Teleseismic data, and they did not provide a 3D image of the overall structure of Iran.

One of the earliest studies about the crustal structure of Iran had been made by Dehgani and Makris (1983) who used gravimetric data to determine the depth of Moho. Mokhtari et al. (2004) used seismic data to determine Moho depth and velocity modeling in the upper mantle. Other studies on crustal depth and tectonic status of Iran can be referred to Taghizadeh et al. (2014) using teleseismic data by P-receiver transfer method. Mousavi and Ebbing (2018) using modeling and inversion of the combination of gravimetric and magnetic data to determine Iran's magnetic basement. Some other studies on the Moho depth of Iran are presented in Table 1, where different locations are compared with each other in eight groups.

In this paper, for the first time, the whole gravimetric data of Iran is used to analyze the 3D structural status of Iran and its Moho depth. These data include scattered gravitational stations available throughout Iran that can be used effectively for large-scale geological and tectonic studies. Terrestrial gravity anomaly map of Iran is shown in Figure 12. The minimum of data is seen in the high Zagros zone, and the maximum of data is seen in the north of the Oman Sea (Makran Zone) and the south of the Caspian Sea.

Table 1. A brief history of Moho depth studies in Iran. (ZFTB: Zagros Folded Thrust Belt, SSZ: Sanandaj-Sirjan Zone, UDZ: Urumieh–Dokhtar Zone, MZT: Main Zagros Thrust, UDMA: Urumieh–Dokhtar Magmatic Arc).

Region	Explanation	depth	Ref
Northeastern Iran Kopeh-Dagh	Talesh mountains and northern Iran	50-60	Shad Manaman et al. (2011)
	Beneath the Kopeh Dagh	~40–45	
Caspian Sea	Kopeh-Dagh Mountains	43 ± 2, and 50 ± 2 km	Taghizadeh et al. (2014)
	The coastal region of the South Caspian Sea	~46	Radjaee et al. (2010)
	South Caspian Basin	30-33	Shad Manaman et al. (2011)
Alborz	Central Alborz zone	54	Sodudi et al. (2009)
	Beneath the Damavand volcano	~67	
	Central Alborz zone	55-58	Radjaee et al. (2010)
	West, and East of Alborz mountains	35-37	Shad Manaman et al. (2011)
	Under the Damavand volcano	~55–60	
	Beneath the Alborz Mountains	50 ± 2	Taghizadeh et al. (2014)
	Near the Damavand volcano	56 ± 2	
Central Iran	The northern part of Central Iran	~48	Radjaee et al. (2010)
	The southern part of Central Iran	~42	Shad Manaman et al. (2011)
	Middle of the Central Iran	~35-42	
	Lut block	35-40	
	Central Iran (ave)	42	Afsari et al. (2011)
	Central Iran	47	Sodudi et al. (2009)
	Beneath the Central Iran	40 ± 2, and 44 ± 2	Taghizadeh et al. (2014)
	Beneath the Iranian plate	40 ± 2 to 45 ± 2	
ZFTB - SSZ	Beneath the MZT	65	Shad Manaman et al. (2011)
	Beneath the SSZ	65	
	Northwest Zagros (ave)	42	Afsari et al. (2011)
	Sanandaj-Sirjan Metamorphic Zone (ave)	51	
	Beneath the ZFTB	43 ± 2	Taghizadeh et al. (2014)
	Beneath the SSZ	50 ± 2–55 ± 2	
Persian Gulf	Under the Persian Gulf	~38	Shad Manaman et al. (2011)
Makran	Oman Sea	18-28	Abdollahi et al. (2018) & (2019)
	Makran fore-arc setting	35-40	
	Western Makran	25-30	Shad Manaman et al. (2011)
	Beneath the Makran highlands	48-50	
	Eastern Makran	~40	
	Makran region	33 ± 2	Taghizadeh et al. (2014)
UDZ	Below the UDMA	~42	Shad Manaman et al. (2011)
	Urmieh-Dokhtar Cenozoic volcanic belt (ave)	43	Afsari (2011)

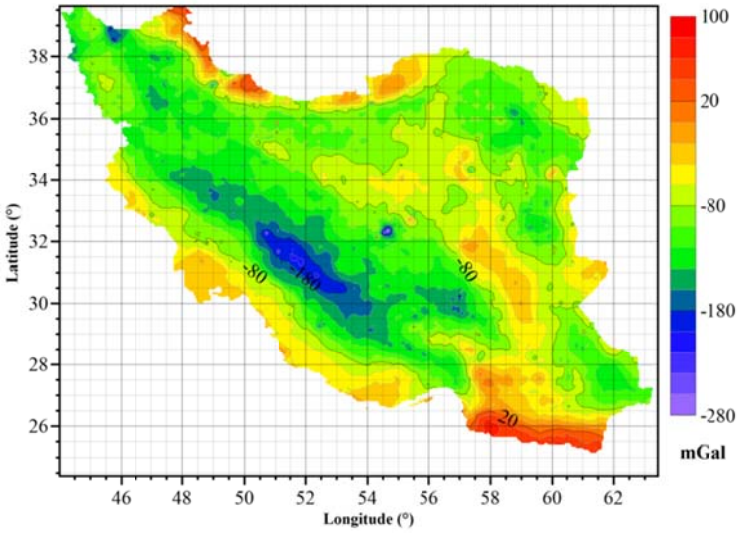

Figure 12. Map of the gravity anomaly of the whole of Iran.

As shown in the figures, there is a good agreement between the Bouguer gravity anomaly trend and trends in the major geological structures of Iran (Figures 11 and 12). For example, the NW-SE trend of the ZFTB is well marked by blue contour in the Bouguer gravity anomaly map. Among the studies done on this zone and related gravity data, the study by Abedi and Oskooi (2015) can be mentioned in which a combination of magnetic data and Bouguer gravity anomaly data inversion is examined, and the tectonic of the area has been discussed.

Now, the results of applying the 3D cross-correlation on terrestrial gravity anomaly of Iran are discussed to identify and intercept major geological structures with increasing depth and the Moho depth. For this purpose, cells of 50×50×10 km^3 are used, and the method was continued to 65 *km* depth. This imaging took 5 minutes approximately for the Intel Core i5-2430M Acer 5750G laptop with 8 GB RAM memory. It should also be noted that for this method, there is no need for an a Priori model and linearization. Figure 13 shows the results of applying the 3D cross-correlation method on terrestrial gravity anomaly data of Iran, and for better representation, the results of the method are shown at depths of 5, 15, 45 and 65 km in Figures 13 and 14.

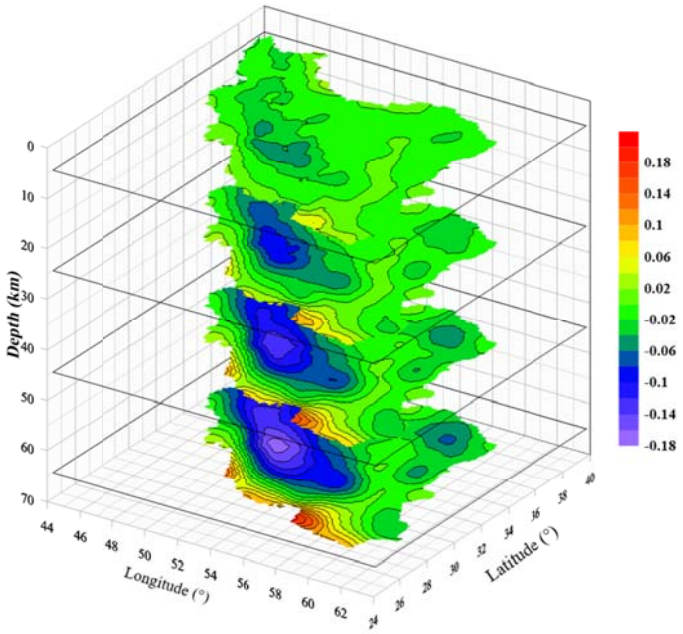

Figure 13. The 3D cross-correlation map of Iran.

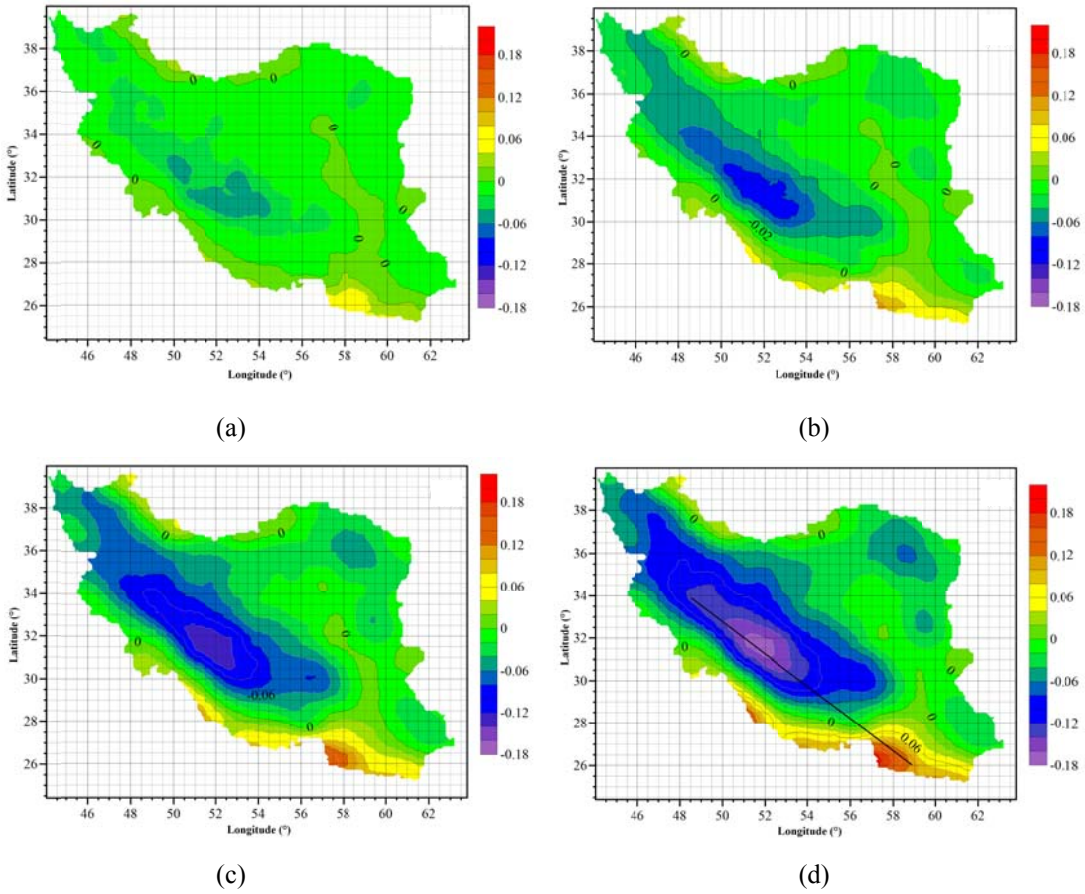

Figure 14. Map obtained by applying the 3D cross-correlation method on gravity anomaly data of Iran at: a) 5 km, b) 25 km, c) 45 km, d) 75 km depth. The black line shows the location of the section of Figure 15.

Here, we discuss the result of the 3D cross-correlation maps at different depths in comparison to the previous studies of the structural zones in Iran. Because of the nature of the method, we must search for the highest absolute values indicating mass excess or mass deficit. Maximum and minimum of cross-correlation values are in the Zagros, Sanandaj-Sirjan and Makran zone. Here, we only discuss the results of applying this approach in these regions. For this purpose, a section is plotted that crosses the Zagros and Makran Zone. The result of this section is presented in Figure 15, and continued to 150 km depth.

By looking at the location of Zagros and Sanandaj-Sirjan zones in the 3D cross-correlation maps (Figures. 13 and 14), it can be noticed that the thickness in the highest location of Zagros mountain is the maximum (absolute value) value, indicating thicker crustal layer in this area. According to 3D correlation maps at different depths, the Moho depth in the upper Zagros is estimated to be 65 km. This result is in agreement with the studies of Dehghani and Makris (1983) and Shad Manaman et al. (2011). Another thing seen in the 3D correlation maps is that Zagros, Sanandaj-Sirjan zones, and Central Iran plateau are joined together down in the depth, and they construct the Iranian continent plate, which has lower density (negative values of 3D correlation) in relation to oceanic plates (Arabian and Turan Plate).

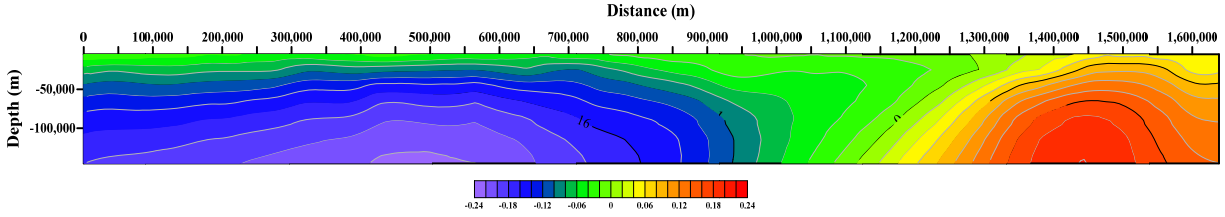

Figure 15. Section map over the Makran Zone and the Zagros zone (axes in this map are in meter unit).

As shown in Figure 14 (a) to (d), Makran zone shows the highest values of the cross-correlation products. It is similar to the gravity map of Iran (Figure 12). This zone is located in the southeastern part of Iran and north of the Oman Sea. The Moho depth map of Iran, using gravimetric studies (Dehghani et al., 1983) shows a thickness of about 40 km for the crust in the northern Makran area, which gradually approaches less than 25 km along the coast of the Oman Sea. However, this research has a different result. The thickness of this zone is well visible in Figures 13, 14, and 15 compared to the other zones. As the depth increases, the positive correlation values increase rapidly, which implies that it has a shallow crust, and it also implies a density increase. As seen in Figure 13, as the depth increases, the correlation values increase, which corresponds to the high-density oceanic crust present in this region extending to high depths. Based on these maps, it can be concluded that the depth of the Moho discontinuity in this region is almost ~20-30 km, which is almost consistent with Taghizadeh et al. (2014) and Abdollahi et al. (2018, 2019) results about this region. It is mentioned that with increasing depth, the Makran zone is extending beneath the Iran plateau toward the Lut block.

Another part of Figure 12, which can be noted as anomaly, is the southern part of the Central Iran Zone. By applying the 3D cross-correlation on it, interesting results can be obtained. This zone that corresponds to the Lut Block, and is in the eastern part shown in Figures 13 and 14 is coincident with 0 value contour. Topographically, the zone is completely flat and desert. According to Figure 12, the gravity anomaly in this region has median values of gravity data, which may belong to intrusive igneous intrusions that have intruded into the continental crust and have risen to near surface. The results of Correlation maps at different depths and correlation values in this area (Figures 13 and 14) show that this anomaly is vanished in the 65 km depth, and zero contour value is gone in 65 km depth. Therefore, it can be concluded that the Moho depth of this zone is 45 km, and this result is almost consistent with the study of Shad Manaman et al. (2011) on this region.

5. Conclusions

In this paper, we introduce and evaluate the 3D gravity cross-correlation method for 3D modeling of the gravity data (or its vertical gradient). This method was applied to three different synthetic models, and its advantages and disadvantages in the modeling of gravity anomaly and vertical gravity gradient data are discussed. The results show the high accuracy of this method in determining the shape and depth of the buried mass. This method is simple, easy to run, and as mentioned above, there is no need for an a priori information, which is the reason that this process is performed at a much faster speed than other commonly used inversion methods and commercial software. Because of that, this method is the fastest method for interpretation of large-scale data set. At the end, for the first time with the help of this method, and for a very short time, the whole terrestrial gravity anomaly data of Iran were seamlessly processed to study the 3D model of the crustal layer beneath the Iranian Plateau and the Moho discontinuity. The results are in agreement with previous works and researches.

References

Inácio, P. and Gunter, B.C., 2010, A Sensitivity Study into Strapdown Airborne Gravimetry. Aerosp. Eng., vol. M.Sc., P. 125.

Alberts, B.A., 2009, Regional gravity field modeling using airborne gravity data. http:// repository.tudelft.nl/assets/uuid: 9c6c7ce7- 7227-4bab-8699-db32697c92a8/Alberts_2009_ phdthesis. pdf.

Braile, L.W., Keller, G.R. and Peeples, W.J., 1974, Inversion of gravity data for two-dimensional density distributions. J. Geophys. Res., 79(14), 2017–2021.

Bear, G.W., Al-Shukri, H.J. and Rudman, A.J., 1995, Linear inversion of gravity data for 3-D density distributions. Geophysics J., 60(5), 1354–1364.

Li, Y. and Oldenburg, D.W., 1998, 3-D inversion of gravity data. Geophysics, 63(1), 109–119, doi: 10.1190/1.1444302.

Talwani, M. and Ewing, M., 1960, Rapid computation of gravitational attraction of three-dimensional bodies of arbitrary shape. Geophysics, 25(1), 203–225.

Cordell, L. and Henderson, R.G., 1968, Iterative three-dimensional solution of gravity anomaly data using a digital computer. Geophysics, 33(4), 596–601.

Oldenburg, D.W., 1974, The inversion and interpretation of gravity anomalies. Geophysics, 39(4), 526–536.

Gómez-Ortiz, D. and Agarwal, B.N.P., 2005, 3DINVER. M: a MATLAB program to invert the gravity anomaly over a 3D horizontal density interface by Parker--Oldenburg's algorithm. Comput. Geosci. J., 31(4), 513–520.

Chakravarthi, V. and Sundararajan, N., 2007, 3D gravity inversion of basement relief—A depth-dependent density approach. Geophysics, 72(2), I23-I32.

Patella, D., 1997, Introduction to ground surface self-potential tomography. Geophys. Prospect., 45(4), 653–681.

Mauriello, P. and Patella, D., 1999a, Principles of probability tomography for natural-source electromagnetic induction fields. Geophysics, 64(5), 1403–1417.

Mauriello, P. and Patella, D., 1999b, Resistivity anomaly imaging by probability tomography. Geophys. Prospect. J., 47(3), 411–429.

Mauriello, P. and Patella, D., 2001, Gravity probability tomography: a new tool for buried mass distribution imaging. Geophys. Prospect. J., 49(1), 1–12.

Alaia, R., Patella, D. and Mauriello, P., 2009, Imaging multipole self-potential sources by 3D probability tomography. Prog. Electromagn. Res. J., 14, 311–339.

Guo, L., Meng, X. and Shi, L., 2010, 3D correlation imaging of the vertical gradient of gravity data. Geophys. Eng. J., 8(1), 6–12.

Plouff, D., 1976, Gravity and magnetic fields of polygonal prisms and application to magnetic terrain corrections. Geophysics J., 41(4), 727–741.

Berberian, M. and King, G.C.P., 1981, Towards a paleogeography and tectonic evolution of Iran: Reply. Can. J. Earth Sci., 18(11), 1764–1766.

Berberian, M., 1983, The southern Caspian: a compressional depression floored by a trapped, modified oceanic crust. Can. J. Earth Sci., 20(2), 163–183.

Stoneley, R., 1981, The geology of the Kuh-e Dalneshin area of southern Iran, and its bearing on the evolution of southern Tethys. J. Geol. Soc. London., 138(5), 509–526.

Richards, J.P., Wilkinson, D. and Ullrich, T., 2006, Geology of the Sari Gunay epithermal gold deposit, northwest Iran. Econ. Geol. J., 101(8), 1455–1496.

Bird, P., 1978, Finite element modeling of lithosphere deformation: the Zagros collision orogeny. Tectonophysics, 50(2–3), 307–336.

Page, W.D., Alt, J.N., Cluff, L.S. and Plafker, G., 1979, Evidence for the recurrence of large-magnitude earthquakes along the Makran coast of Iran and Pakistan. Tectonophysics, 52 (1–4), 533–547.

Dehegani, G.A. and Makris, J., 1983, The gravity field and crustal structure of Iran. Geodynamic project (Geotraverse) in Iran. Neues Jahrbuch Geologie und Palaeontologie, Abhandlungen.

Mokhtari, M., Farahbod, A. M., Lindholm, C., Alahyarkhani, M. and Bungum, H., 2004, An approach to a comprehensive Moho depth map and crust and upper mantle velocity model for Iran. Iran. Int. J. Sci., 5(2), 223–244.

Taghizadeh-Farahmand, F., Afsari, N. and Sodoudi, F., 2015, Crustal thickness of Iran inferred from converted waves. Pure Appl. Geophys., 172(2), 309–331.

Mousavi, N. and Ebbing, J., 2018, Basement characterization and crustal structure beneath the Arabia--Eurasia collision (Iran): a combined gravity and magnetic study. Tectonophysics, 731, 155–171.

Shad Manaman, N., Shomali, H. and Koyi, H., New constraints on upper-mantle S-velocity structure and crustal thickness of the Iranian plateau using partitioned waveform inversion. Geophys. J. Int., 184(1), 247–267.

Radjaee, A., Rham, D., Mokhtari, M., Tatar, M., Priestley, K. and Hatzfeld, D., 2010, Variation of Moho depth in the central part of the Alborz Mountains, northern Iran. Geophys. J. Int., 181(1), 173–184.

Sodoudi, F., Yuan, X., Kind, R., Heit, B. and Sadidkhouy, A., 2009, Evidence for a missing crustal root and a thin lithosphere beneath the Central Alborz by receiver function studies. Geophys. J. Int., 177(2), 733–742.

Afsari, N., Sodoudi, F., Farahmand, F.T. and Ghassemi, M.R., 2011, Crustal structure of northwest Zagros (Kermanshah) and Central Iran (Yazd and Isfahan) using teleseismic PS converted phases. J. Seismol., 15(2), 341–353.

Abdollahi, S., Ardestani,V.E., Zeyen, H. and Shomali, Z., 2018, Crustal and upper mantle structures of Makran subduction zone, SE Iran by combined surface wave velocity analysis and gravity modeling. Tectonophysics, 747, 191-210.

Abdollahi, S., Zeyen, H., Ardestani, V.E. and Shomali, Z., 2019, 3D joint inversion of gravity data and Rayleigh wave group velocities to resolve shear-wave velocity and density structure in the Makran subduction zone, southeast Iran. Journal of Asian Earth Sciences, 173, 275-290.

Abedi, M. and Oskooi, B., 2015, A combined magnetometry and gravity study across Zagros orogeny in Iran. Tectonophysics, 664, 164–175.